

Article

# Passability and Internode Mechanics Analysis of a Multisection Micro Pipeline Robot

Shengtao Chen <sup>1,2,3,\*</sup>, Kai Teng <sup>1</sup>, Kang Zhang <sup>1</sup>, Xiaolu Wang <sup>1</sup>, Lei Xia <sup>1</sup>, Meiyu Zhang <sup>1</sup>, Yibo Zhang <sup>1</sup>  
and Yongjun Gong <sup>1,2,3,\*</sup>

<sup>1</sup> College of Naval Architecture and Ocean Engineering, Dalian Maritime University, Dalian 116026, China

<sup>2</sup> Liaoning Provincial Key Laboratory of Rescue and Salvage Engineering, Dalian Maritime University, Dalian 116026, China

<sup>3</sup> International Joint Research Centre for Subsea Engineering Technology and Equipment, Dalian Maritime University, Dalian 116026, China

\* Correspondence: dutchshengtao@sina.com (S.C.); dmucst@dlnu.edu.cn (Y.G.)

**Abstract:** In submarine oil and gas pipelines, the movement of a differential pressure multisection pipeline robot mainly relies on the front and rear driving pressure difference of the fluid and the friction between the cup and the pipe wall. The passability of the pipeline is a key point to guarantee success in scanning and detecting the inner wall of a pipeline by robot. When the multisection pipeline robot moves, the force of the internode connection points changes the degree of freedom of the robot. The existence of the connection points causes speed fluctuations in the robot during the movement process which, in turn, affects the detection accuracy of the pipeline. Consequently, a systematic analysis of the connection point movement is of great importance. In this paper, a rigid-flexible, coupled, multibody, dynamic motion system is established, where a multisection micro pipeline robot is built. The cup of the robot is set as a flexible body. The motion law of the differential pressure multisection pipeline robot is analyzed through simulation, and the robot's motion speed and internode stress of the different cabin sections are explored jointly in practice. Taking the transportation of an oil and gas pipeline into full consideration, the motion law and force of the multisection pipeline robot are analyzed by changing the bulge and turning the radius of the inner wall of the pipeline. A corresponding experimental bench is built to explore the effects of different numbers of cups and lengths of the cabin sections on the turning characteristics of the robot. Simulations and experiments results are highly similar and within the error range. To this end, the presented work provides significant information for the model selection of multisection micro pipeline robots in the fields of submarine oil and gas pipelines.

**Keywords:** multisection pipeline robot; universal joint; turning radius; force analysis



**Citation:** Chen, S.; Teng, K.; Zhang, K.; Wang, X.; Xia, L.; Zhang, M.; Zhang, Y.; Gong, Y. Passability and Internode Mechanics Analysis of a Multisection Micro Pipeline Robot.

*Actuators* **2023**, *12*, 137. <https://doi.org/10.3390/act12040137>

Academic Editors: Myun Joong Hwang and Maolin Jin

Received: 13 February 2023

Revised: 20 March 2023

Accepted: 22 March 2023

Published: 24 March 2023



**Copyright:** © 2023 by the authors. Licensee MDPI, Basel, Switzerland. This article is an open access article distributed under the terms and conditions of the Creative Commons Attribution (CC BY) license (<https://creativecommons.org/licenses/by/4.0/>).

## 1. Introduction

In recent years, with the development of industry and the needs of people, submarine pipelines are widely used to transport oil and gas to domestic resource supplies, nuclear industry and other fields [1]. The oil industry grew tremendously in the 1970s, and pipeline engineering followed on a large scale. In the 1950s, the first pipeline robot propelled by fluid pressure was developed, which was also called a PIG (Pipeline Inspection Gauge) due to its shape. A PIG is driven by fluid to achieve movement and obtain speed through the pressure difference between the front and rear of the robot, and it is controlled through other equipment to complete inspections of the inner diameter of the pipe and for cleaning the pipe wall [2–5]. Yang et al. developed a robot that generates electricity during a pipeline's operation. It is mainly composed of three parts: body, power generation and guidance. The power generation part is used to realize the power supply function of the whole device, mainly to convert the kinetic energy generated by the impeller due to the impact of the fluid into the electric energy of the battery; the main body of the robot adopts the support

wheel, the control platform and the power supply group, which can realize the robot's walk along the pipe's wall in the pipeline. The traction mechanism uses the guidance of the electromagnet and the guide head to enable the robot to pass curves smoothly [6]. Some companies jointly developed a robot with the ability of pipe diameter adaptation that can be driven by fluid to move forward and backward freely to remove pipe attachments. Two drive cups are arranged symmetrically at both ends of the PIG to realize the two directions of the PIG; at the same time, the PIG is loaded with two sets of elastic support wheels, and the corresponding cups are arranged in the middle of the PIG to prevent eccentric conditions caused by the weight of the PIG and to ensure a seal for operation [7].

Several researchers have experimented with bypass pigging techniques for PIG kinetic studies [8–10]. Frank Kirchner developed a MAKRO robot, which uses a roller to walk. Based on the stability of the hinge connection during bending, the robot's passability and obstacle-crossing ability were simulated [11]. This type of robot is more demanding in terms of smoothness of the pipe and less stable when passing through the bumps and grooves in the inner wall of the pipe, and it is difficult to guarantee the movement speed. Young-Sik et al. developed a differential pipeline inspection robot whose performance is driven by a telescopic rotating rod and can perform inspection functions inside the pipeline [12]. This type of robot drive is simple and convenient, but the structure is more complex, and the telescoping mechanism is prone to jamming during the bending process. Atsushi et al. designed a pipeline robot that adapts to a small orifice diameter. The dynamic characteristics of the spiral mechanism were analyzed, and the relationship between the spring stiffness, motor torque, robot length and static friction of the pipe wall was obtained [13]. Gleicher et al. adopted the CEL fluid–structure interaction volume method to simulate the deformation and equivalent stress of the skin bowl under fluid driving [14]. Ducobu et al. performed simulations of the CEL fluid–structure coupling, and the surface method was used to analyze the motion characteristics of their robot under non-weld conditions and the deformation of the skin bowl driven by the fluid [15]. Xue et al. established the CEL model of a PIG, explored the influence of the thickness and hardness of the cup on the friction and analyzed the blockage caused by the robot during the movement process [16]. Hendrix et al. adopted a self-developed experimental device that uses a steel hull to study a two-way PIG and the ratio between the friction and contact force [17]. Reinforcement learning has been widely used to control robots to cultivate a self-learning ability. Goharimanesh et al. applied fuzzy reinforcement learning to the continuous control of robots. In addition, the genetic algorithm was used to adjust the control parameters to improve the stability and trajectory tracking ability of the robot [18]. Ignacio et al. designed an adaptive PID controller for a mobile robot and evaluated the PID parameters through simulation experiments and control [19]. The solid–fluid coupling-based approach to leather bowl stress and friction analysis for the above robots is more comprehensive, but the research in multisectional pipe robots still leaves many gaps.

Low-flow pipeline robots have been widely used in submarine oil and gas pipelines in recent years [20]. A few studies have focused on the running speed, wall friction and dynamic characteristics [21–23]. Experts have conducted a large amount of research on the frictional contact behavior between the PIG cup and the straight pipe [24,25]. Wang et al. analyzed the force state and the theoretical calculation of the cup during the operation of the PIG with the help of two-dimensional diagrams and provided a series of suggestions for the design of the PIG [26]. Zhang et al. used the finite element method to analyze the mechanical properties of the pig cup and obtained the factors that affect the contact stress and bending stress of the robot cup under different working conditions [27,28]. Zhang et al. predicted the contact force of bidirectional PIG and discussed the effects of cup interference, cup thickness, cup curvature and the size of contact with the tube wall on the contact force of the cup at different pressure differentials [29–31]. Narmak analyzed the motion state of a robot in an oil and gas pipeline using the numerical simulation method, obtained the pressure distribution of the fluid along the pipeline and studied the robot's movement in the oil and gas pipeline [32]. Zhu et al. considered the interference contact between

the sealing cup and the inner wall of the pipe and established an axisymmetric dynamic model of the interaction system of the cabin (rigid body)–seal cup (super elasticity)–inner wall of the pipe, and they predicted the contact force between the pipeline robot and the inner wall of the pipeline [33,34]. The shock vibration and speed control of pipeline robots have been studied for many years. Den Heijer et al. combined the linear elastic contact model with a nonlinear Reynolds equation to determine the coefficient of friction and contact force under lubricated conditions [35]. Liang et al. proposed that the instrument of the pipeline inspection braking unit can be used to control the speed of the PIG. In this method, the Euler–Cauchy method is used to solve the speed control equations in different situations [36]. Miao et al. analyzed the motion of PIG by establishing a nonlinear dynamic model and using dynamic simulation and proposed a WOA controller to reasonably control the motion speed [37]. Kim et al. proposed two new friction PIG models, mainly to study the speed offset caused by friction and to predict the movement speed and working time of the robot in a long pipeline system. Currently, there are more studies on the pigging effect of pipeline robots [38]. Li et al. simulated and analyzed the flow field around a PIG and determined that the friction force is the main force affecting the movement of the PIG [39]. Liu et al. combined OLGA and CFD simulations, and the bypass pigging method was adopted to alleviate pipeline obstructions and improve the speed of a robot's operation [40]. Chen et al., based on the CFD method, performed a numerical simulation to explore the influence of gas–liquid two-phase flow in the clearance between the PIG and the tube wall on the pigging effect of a PIG [41]. Cao et al. established a PIG with a single section length of 269 mm and a diameter of 206 mm for a large pipe with an internal diameter of 249 mm and investigated the effect of the flow field on the PIG emission and the effect of contact behavior [42]. Based on the above pipeline robots, we found that they work in a single way, so we adopted fluid drive to explore the differential pressure multisection pipeline robots that can integrate cleaning and inspection functions. These robots are simple in structure, easy to drive and suitable for pipes of different diameters. Moreover, the robots use leather bowl contact, which is less likely to cause jamming, and are connected by a cross universal coupling in the middle, which enhances the efficiency and stability of the robots. Meanwhile, according to the above PIG studies, researchers have conducted a comprehensive study on robot skin bowl friction and speed control, but there are fewer studies on multisectional robots, and there are mostly gaps in the study of skin bowl forces and connections for multisectional robots.

Therefore, in this paper, a pipe robot with a single section length of 60 mm and a diameter of 50 mm was constructed. This paper used ADAMS and set the leather bowl as a flexible body. We explored the effect of changing the number of cabins, the bulge height of the inner wall of the pipeline and the turning radius of the pipeline on the motion law of a robot and the force at the connection point of the universal joint. In addition, by building a corresponding experimental bench, we explored the influence of changing the number of cabins and the number of cups on the movement of the robot.

## 2. Finite Element Model Validation

### 2.1. Theoretical Analysis

In the process of movement, a multisection pipeline robot has the most obvious force at the bending stage. Figure 1 shows a force diagram of a two-section pipeline robot at the bending stage, which mainly includes the pressure of the pipe inlet and outlet, the supporting force of the pipe wall on the robot and the friction force between the robot and the pipe wall. Figure 2 shows the local stress diagram of the leather bowl after stress deformation, which mainly manifests in the friction force at the leather bowl and the bending moment between the leather bowl and the robot's main core tube. Area A in the figure is the inner wall of the core tube, and the marked length is the position of the normal torque generated between the leather bowl and the core tube.

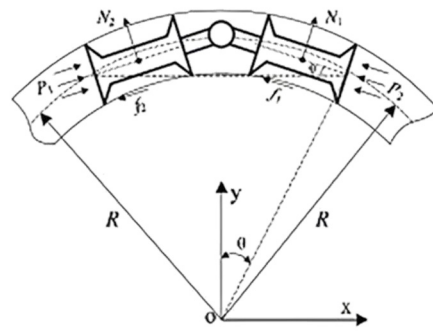


Figure 1. Force diagram of the two-section robot.

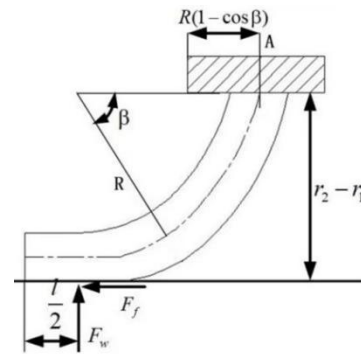


Figure 2. Force diagram of the leather bowl.

The pressure on a working pipeline robot during work is evenly distributed, relying on the front and rear pressure difference to move forward. Assuming that the positive pressures of the two cups of the pipeline robot are equal, the formula can be written as follows:

$$N_1 = N_2 = \frac{1}{2} \int_0^l q(x)dx = \frac{1}{2} \int_0^l \frac{\rho v^2}{2R} A(x)dx = \frac{\rho v^2}{4R} \int_0^l A(x)dx \tag{1}$$

where  $N_1$  and  $N_2$  represent all the bowls that are subjected to the combined force of the pressure from the inner wall of the pipe, Newton;  $R$  is the pipe turning radius, mm;  $\rho$  is the PIG density, kg/m<sup>3</sup>;  $l$  is the PIG length, mm;  $v$  is the PIG speed, m/s; and  $A(x)$  is the pipeline cross-sectional area, mm<sup>2</sup>. Further, the friction force on the upper cup of the pipeline robot is:

$$f_1 = f_2 = \mu(N_1 + N_2) = \frac{\mu \rho v^2}{2R} \int_0^l A(x)dx \tag{2}$$

where  $f_1$  is the resultant force of the friction on the end bowl, Newton;  $f_2$  is the resultant force of the friction on the front leather bowl, Newton; and  $\mu$  is the friction coefficient. To ensure the smooth operation of a robot in a pipeline, the energy conservation and equal torque should be followed. As shown in Figure 2, the friction torque on the cup is:

$$M_f = F_f(r_2 - r_1)r_2d\theta \tag{3}$$

The normal force of the front cup during operations is:

$$P_{1y} = (P_1 - f_1)\sin\theta = P_1\sin\frac{l}{2R} - \mu N_1\sin\frac{l}{2R} - \frac{\rho v^2}{2R}\sin\frac{l}{2R} \int_0^l A(x)dx \tag{4}$$

$$M_w = F_w \left[ \frac{l}{2} + R(1 - \cos(\beta)) - \frac{t\cos\beta}{2} \right] rd\theta \tag{5}$$

$$q(x) = ma_n = \rho A(x) \frac{v^2}{R} = \rho A(x)\omega^2 R \tag{6}$$

The axial force and moment when the front end cup is running are:

$$P_{1x} = (P_1 - f_1)\cos\theta = P_1\cos\frac{l}{2R} - \mu N\cos\frac{l}{2R} \frac{\mu\rho v^2}{2R} \int_0^l A(x)dx \quad (7)$$

$$M_b = \int \sigma_b x dx R d\theta \quad x = \Delta P \sin(\beta) \quad (8)$$

$$M_{\Delta P} = \Delta P \left(R - \frac{t}{2}\right)^2 d\theta \left[ \frac{\beta - \sin(\beta)\cos(\beta)}{2} \left(R - \frac{t}{2}\right) + r_2(1 - \cos(\beta)) \right] \quad (9)$$

Solving the above equation can deduce the force of the rear cup as follows:

$$P_{2x} = -P_2\cos\frac{l}{2R} - \mu N\cos\frac{l}{2R} - \cos\frac{l}{2R} \frac{\mu\rho v^2}{2R} \int_0^l A(x)dx \quad (10)$$

$$P_{2y} = -P_2\sin\frac{l}{2R} - \mu N\sin\frac{l}{2R} - \frac{\rho v^2}{2R} \sin\frac{l}{2R} \int_0^l A(x)dx \quad (11)$$

$$M_f + M_w - (M_{\Delta P} + M_b) = 0 \quad (12)$$

where  $r_1$  is the tank section radius, mm;  $r_2$  is the pipe diameter, mm;  $P_1$  is the inlet thrust, Newton;  $P_2$  is the outlet thrust, Newton;  $M_f$  is the leather bowl friction torque, N·m;  $M_w$  is the normal torque, N·m;  $M_{\Delta P}$  is the moment of the fluid differential pressure, N·m;  $M_b$  is the leather bowl bending moment, N·m;  $F_w$  is the normal load, N;  $\beta$  is the leather bowl deformation rate;  $\theta$  is the section pass rate;  $\sigma_b$  is the contact stress, N;  $P_{1x}$  is the axial force of the front leather bowl, MPa;  $P_{2x}$  is the axial force on the back leather bowl, MPa;  $P_{1y}$  is the normal force on the front leather bowl, MPa;  $P_{2y}$  is the normal force on the back leather bowl, MPa;  $t$  is the thickness of the cup, mm;  $\omega$  is the angular velocity, rad/s; and  $a_n$  is the centripetal acceleration, m/s<sup>2</sup>.

## 2.2. Model Verification

In order to ensure the accuracy and rationality of the simulation, it was necessary to verify the model. Firstly, a finite element model was established in Abaqus, as shown in Figure 3. Due to the complex structure of the two-section pipe robot, without affecting the calculation results, the model was simplified, and the less influential parts such as fillets and threads were deleted. The number of robot grids reached 13,529. The results of the finite element analysis and dynamic simulation are shown in Figure 4. The changes in the friction force under different thicknesses of the leather bowl were fitted by Origin. The abscissa was the shrinkage rate at the leather bowl, and the ordinate was the friction force generated between the leather bowl and pipe wall. In the initial motion stage of the robot, the error was relatively obvious due to the large, instantaneous driving force. The effect of local deformation generated during the leather bowl motion in the finite element analysis was small and neglected in the dynamic simulation. Therefore, a slight deviation occurred between model validation. Through a comparison of the dynamic model and finite element analysis, the bowl remained consistent under a certain shrinkage rate, which ensured the accuracy and rationality of the dynamic model.

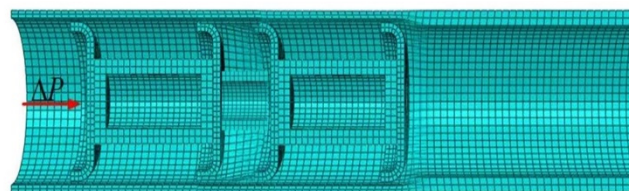


Figure 3. Finite element model of the two-section pipeline robot.

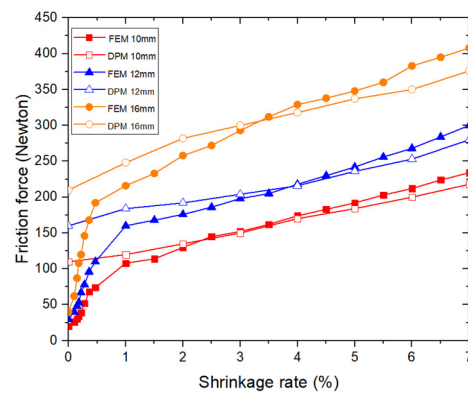


Figure 4. Comparison of the finite element and dynamic models.

During the movement of the pipeline robot, the leather bowls are deformed under pressure. To increase the scientific validity of the simulations and experiments, the leather bowls were made of polyurethane. Therefore, stress verification of the polyurethane leather bowls was needed to meet the experimental requirements. The leather bowl model parameters and physical parameters are shown in Figure 5. In the figure,  $R_B$  is the radius of the leather bowl,  $R_T$  is the radius of the rigid body through-hole,  $r_B$  is the radius of the rigid body and  $L_B$  is the total length of the rigid body. The physical parameters of the leather bowl are shown in Table 1.

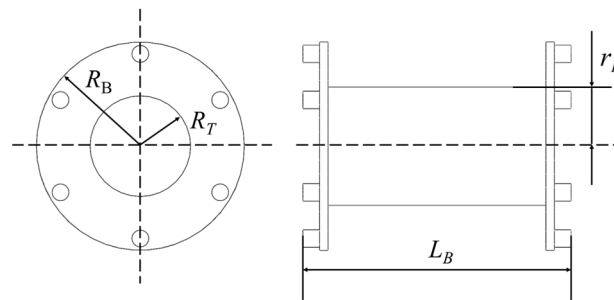


Figure 5. Leather bowl model parameters.

Table 1. Physical parameters of sealing cup.

Physical Quantities	Numerical Value
Density	1.25 kg/m <sup>3</sup>
Young's modulus	3.5 MPa
Poisson ratio	0.49

The situation inside the pipeline is very complex, and the leather bowl, as an element in direct contact with the inner wall of the pipeline, needs to have excellent performance. Stress–strain analysis of the skin bowl, and reasonable structural design and optimization for the area of high stress, can avoid the failure of the skin bowl during operation inside the pipe. In this section, the simulations of the power and drive bowls are performed. Computed results in straight and bending conditions are separately given in Figures 6 and 7. In addition, the averaged stress over the bowl domain is provided in Figure 8. The average stress on the bowl is shown in Figure 8.

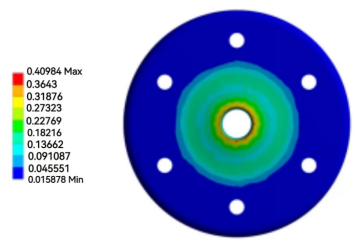


Figure 6. Skin bowl stress in straight pipe.

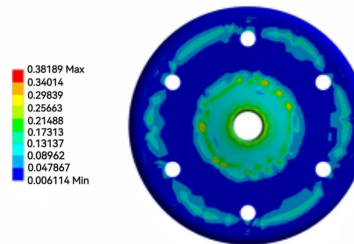


Figure 7. Skin bowl stress in the bend.

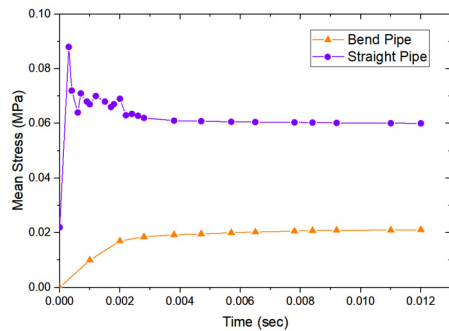


Figure 8. Mean stress of the bowl.

According to the above figure, the stress of the leather bowl was relatively obvious at the rigid body connected in the middle, and the edge was also subjected to obvious stress in the bending process. In addition, the average stress of the leather bowl in the bending tube changed greatly, but the overall stress was small, which met the experimental requirements. Figure 9 shows the average stress of polyurethane leather bowl during bending under different pressures.

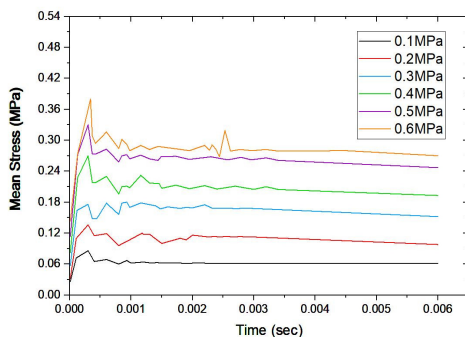


Figure 9. Average stress of leather bowl under different pressures.

As shown in the figure, the average stress of the urethane leather bowl was positively correlated with the fluid pressure during movement, and the stress changes were small, which met the requirements of the simulation and experiment.

### 3. Passability Research

In practical engineering, the structure of the pipeline robot has a great influence on its passability. For example, in an actual situation, robots with different numbers of cabins are used to complete the corresponding work. The inside of a pipeline has different heights from bulges due to processing errors. The complex terrain of a submarine pipeline restricts the regular laying of the pipeline, and a pipeline with different radii appears. These affect the motion law and mechanical properties of the robot. It is necessary to carry out dynamic simulations to objectively and accurately explore the movement of a PIG in the pipeline and to solve the problem of the passability of the robot when passing through a curved pipeline.

#### 3.1. The Effect of the Number of Cabins on the Speed

The pipeline robots developed by most companies mainly have two sections or three sections, and they can complete various functions, such as cleaning and inspection. Under normal circumstances, the movement laws and speed changes of robots with different numbers of cabins are also significantly different. Therefore, it was necessary to perform a motion analysis on robots with different numbers of segments. A pipeline with an inner diameter of 50 mm and a turning radius of 500 mm was used. The model was established in ADAMS, and the leather bowl was converted into a flexible body with Ansys. The Poisson's ratio was 0.49, a band constraint was adopted on the robot's body and a universal pair was used to connect cabin sections. An elastic contact between the leather bowl and pipe wall was set, with a friction coefficient of 0.8 and a recovery coefficient of 0.3. A two-section pipeline robot and a three-section pipeline robot with the same cup structure were supplied with a pressure of 5 MPa, as shown in Figure 10. The influence of the different numbers of cabin sections on the speed and contact force of the robots is shown in Figures 11 and 12.

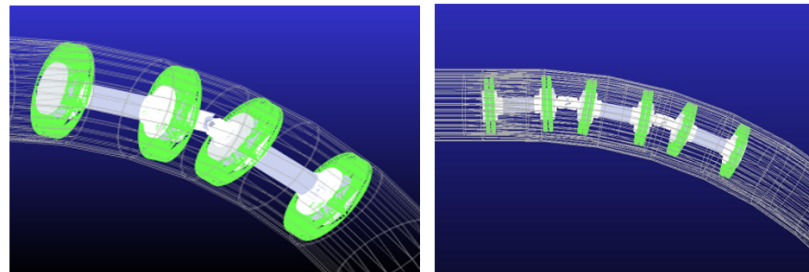


Figure 10. Pipe robots with different numbers of sections.

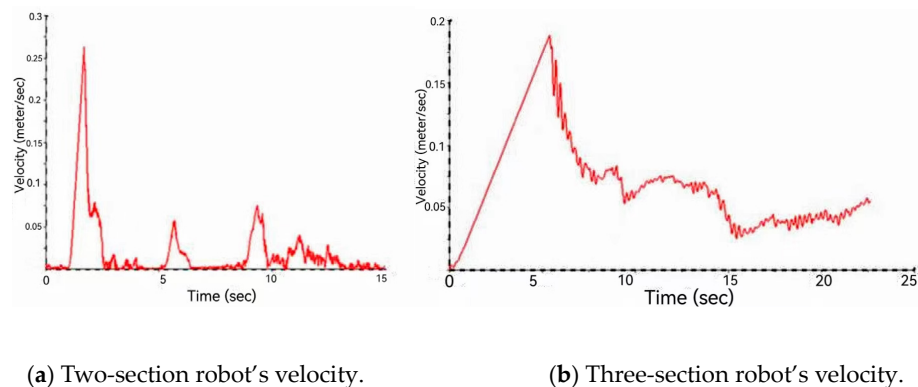
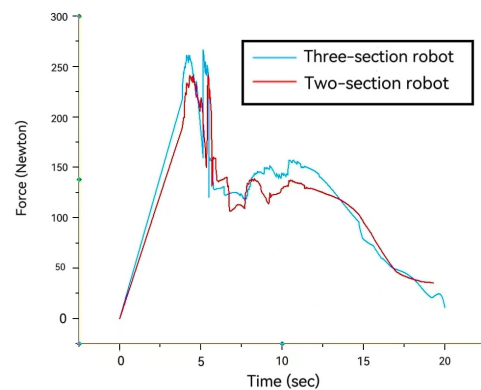


Figure 11. Movement speed of the pipeline robots with different numbers of sections.



**Figure 12.** Contact force of leather bowl with different numbers of compartments.

Through an ADAMS simulation analysis, it could be seen, as shown in Figure 11, that the variation laws of the motion speeds of the two groups of pipeline robots were almost the same. Affected by the initial force, the two groups of robots had a uniform increase in speed in the straight pipe. At the moment of entering the curve, due to the contact force and friction force, the speed dropped sharply. After entering the curve, the speed of the robot increased significantly due to the backlog of pressure and then decreased until it left the pipe. However, the average speed of the two-section robot was 0.12 m/s, and the maximum speed before entering the bend was 0.27 m/s. The average speed of the three-section robot was 0.08 m/s, and the maximum speed before entering the bend was 0.18 m/s. The movement speed of the three-section robot was much lower than that of the two-section one. As shown in Figure 12, a point was taken at each of the two robot leather bowls for monitoring, and the trend of contact force variation at the leather bowls was approximately the same. However, the contact force at the leather bowl of the three-section pipeline robot was slightly higher than that of the two-section pipeline robot because of more constraints on the degrees of freedom of the three-section pipeline robot. According to the force formula of robot motion:

$$(P_1 - P_2)A(x) - F_f - F_w \pm G\sin\theta = m \frac{dv}{dt} \quad (13)$$

where  $F_f$  is the friction of the leather bowl, N; and  $G$  is the PIG gravity, N.

The increase in the number of segments led to an increase in the overall mass of the robot. At the same time the number of leather bowls doubled, which increased the frictional resistance and seriously reduced the robot's movement speed. Additionally, the universal coupling transferred forces to the rear half of the curve when turning, which affected the turning speed of the whole robot. Therefore, in practical engineering, a separate power system is required to prevent the jamming of the robot and monitor the robot's working position and motion status.

### 3.2. The Influence of the Number of Cabins on the Force of the Connection Point

Under normal circumstances, the joints of a multisection pipeline robot are connected by a cross universal coupling. The coupling is subjected to loads in different directions before and after the coupling, which can easily cause deformation of the coupling. The force of the coupling is particularly important. Taking a pipeline with an inner diameter of 50 mm and a turning radius of 500 mm, ADAMS was also used for simulations. The leather bowl and pipe wall were in elastic contact, the universal pair and the core tube were bound by a bond, the parameter settings remained unchanged and 5 MPa pressure was passed into the entrance. A simulation analysis of the pipeline robots with two cabins and three cabins was carried out, and the force change at the center point of the cross was taken, as shown in Figure 13.

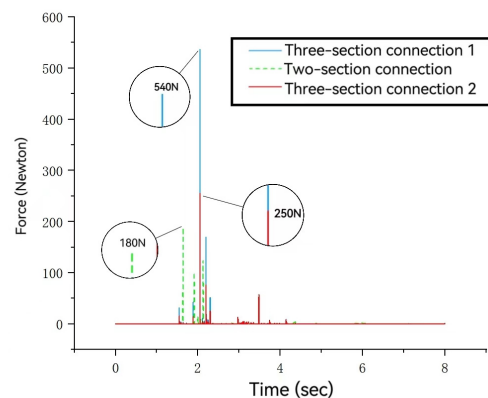


**Figure 13.** Force change at the center of the cross.

The two-section and three-section pipeline robots passed through the pipeline successively, and the simulation results, after ensuring that the number of cabins was the only variable, were as shown in Figure 13. The movement speed of the two-section robot was higher than that of the three-section robot; therefore, the two-section pipeline robot was given priority. Upon entering the pipeline, when the current cabin section bends, there is a large contact force and friction force with the pipe wall, and the speed decreases instantaneously, while the rear section maintains the original speed and continues to move forward, resulting in a large, instantaneous squeeze between the two. According to the ADAMS simulation analysis results, as shown in Figure 13, the curve represents the contact force at the joint point. The instantaneous contact force at the connection point can reach 180 N. For the three-section pipeline robot, when the number of cups increased, the resistance when cornering was significantly higher than that of the two-section pipeline robot. Therefore, the speed difference between the cabin sections was large, resulting in an increase in the extrusion at the connection point and a greater contact force. It can reach 540 N, which causes the overall movement speed to decrease, and the force at the rear connection drops in a ladder shape. The instantaneous contact force at the rear reached 250 N, which exceeded the instantaneous contact force at the connection of the double cabin. In summary, the higher the number of sections, the higher the force at the first PIG connection. The instantaneous contact force at the PIG connection with more sections is also greater. The coupling between the two sections of the robot mainly drives the driven shaft to rotate in a vertical axis through the driving shaft. According to the mechanical formula of the coupling:

$$T_1'' = 2R \times F_1'' = 2R \times F_1 \times \sin\gamma \times tg\varphi \quad (14)$$

where  $T_1''$  is the coupling drive shaft torque, N·m;  $F_1''$  is the coupling drive shaft pressure, N;  $\gamma$  is the coupling drive shaft change rate; and  $\varphi$  is the coupling drive shaft change rate.

Regardless of the deviation between the actual processing and installation, the greater the bending angle during the bending process, the greater the force required by the active axis which, in turn, affects the movement speed and force of the robot.

### 3.3. Vibration Force of the Bending Coupling

Under normal circumstances, a multisection robot vibrates due to the change in the flow field when cornering. The multisection pipeline robot generates obvious contact force during the cornering process, and the coupling generates weak vibration due to the speed change of the robot force. Take a pipe with a length of 500 mm and an inner diameter of 50 mm as an example. Simulated by ADAMS, the connection and parameter settings were kept constant. For the simulation analysis, the inlet pressure was set to 3 MPa, and the two sections of the pipe robot were subjected to forces in X, Y and Z directions, as shown in Figure 14.

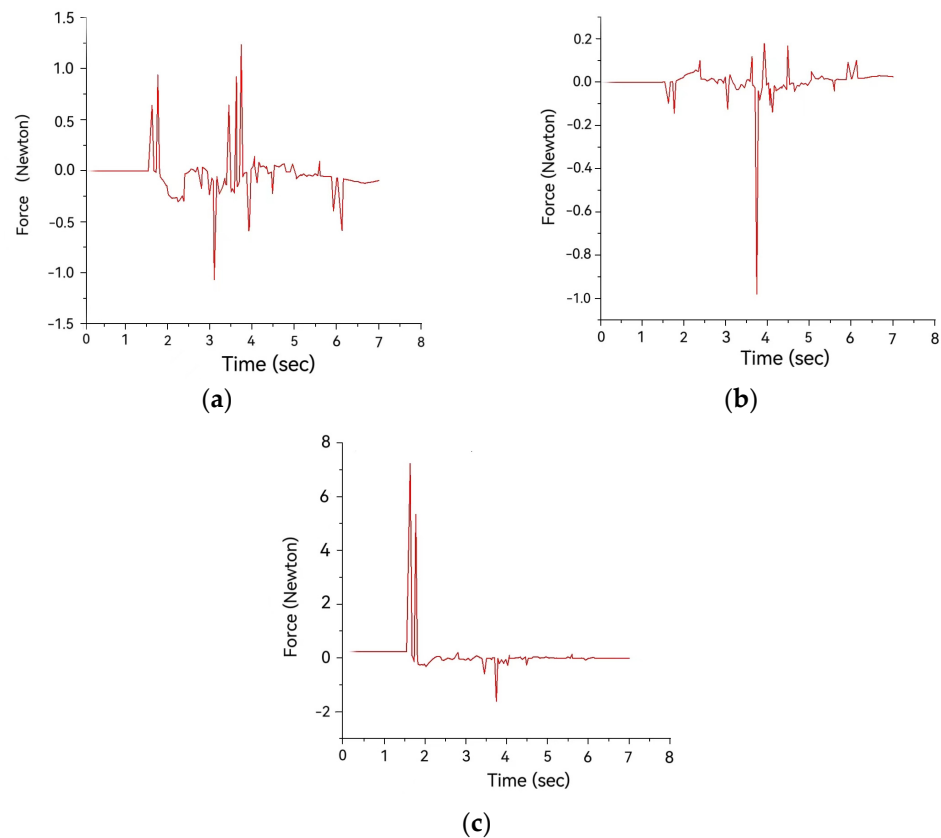


**Figure 14.** When the coupling was bent, the force was applied along the  $x$ –,  $y$ – and  $z$ –axis. (a) Vibration force in the  $x$ –axis direction. (b) Vibration force in the  $y$ –axis direction. (c) Vibration force in the  $z$ –axis direction.

It can be seen from Figure 14a,b that the two-section pipeline robot was accompanied by slight, reciprocating, irregular vibrations along the  $x$ – and  $y$ –axis during the movement process, which mainly manifested as a large vibration amplitude, although the force was relatively high when performing small corner movements. As shown in Figure 14c, a large contact force appeared in the  $z$ –axis direction and was concentrated in the positive direction of the  $z$ –axis. It indicates that the contact force is more concentrated in the same direction at the moment the robot enters the bend. The maximum force at the connection point is likely to cause the universal joint to break.

### 3.4. The Effect of Pipe Bulges on the Robot

In actual working conditions, the inside of a pipe wall bulges due to rust or machining errors, which is also unavoidable. During the movement of the robot, a large stress occurs at the cup and the universal joint, which needs to be simulated and analyzed. Taking a pipe with an inner diameter of 50 mm and a turning radius of 500 mm, a two-section pipeline robot with four cups converted the cup into a flexible body, and it was imported into the simulation, while the friction coefficient and recovery coefficient remained unchanged. The elastic contact between the leather bowl and the pipeline was still adopted to ensure that the height of the bulge was the only variable; the pressure of the pipeline inlet was 5 MPa, and 5, 10 and 15 mm bulges were set at the bend for the simulation. The maximum stress at the universal joint is shown in Figures 15 and 16.

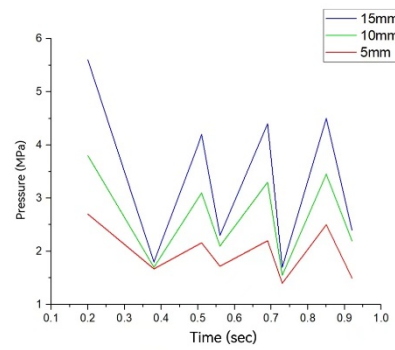


Figure 15. Maximum stress at the different raised cups.

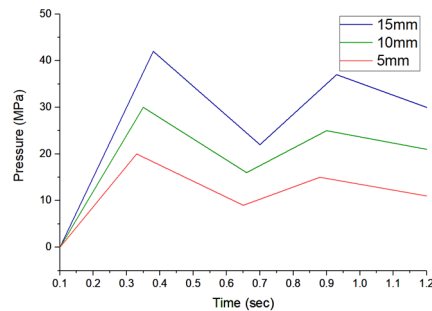


Figure 16. Maximum stress of the different raised universal joints.

Figure 15 shows the maximum stress generated when the leather cup passed through the bulge. Under the premise of ensuring that the robot moved at a constant speed in the pipeline, the first leather cup had the maximum contact stress when it bent. During the bending process, it was affected by the front leather cup. The two leather cups and the third leather cup had greater contact with the outer wall surface of the pipeline; thus, the contact force of the leather cup was small when it passed through the protrusion. A larger contact force was generated, and the leather cup was subjected to a larger contact stress when it passed through the bulge. According to the contact mechanics formula of the cup:

$$dF_N = dG \times \sin\theta = \frac{G \cos\beta \times \sin\theta}{2\pi N} d\theta \tag{15}$$

$$F_N = \int_0^{2\pi} \frac{G \cos\beta \times \sin\theta}{2\pi N} d\theta = 0 \tag{16}$$

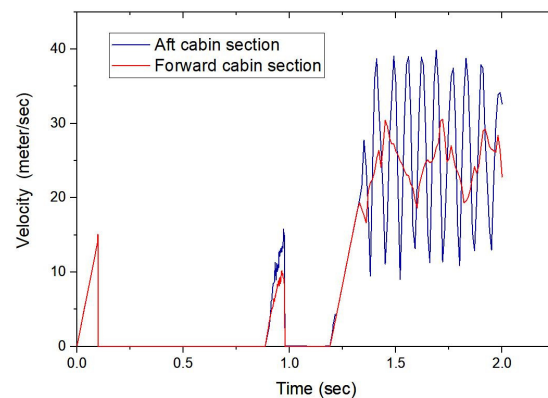
With the increase in the bulge and a larger angle, the contact stress of the leather cup also increases significantly; at the same time, with the increase in the number of compartments, the increase in the gravity also increases the contact stress of the leather cup.

Figure 16 shows the stress change in the universal joint when it passed through the bulge. When the robot passed through different heights of bumps, the trend of force on the universal joint was approximately the same. As the height of the bump increased, the force on the universal joint gradually increased. Maximum stress occurred when the robot passes over a 15 mm bump. When the first cup passed through the bulge, the positions of the two front and rear robots greatly inclined, resulting in a gradual increase in the universal joint’s force; the peak value reached 42 MPa, and the force decreased after passing. During the cornering process, when the other cups passed through the bulge, the position of the robot changed slightly; therefore, the stress on the universal joint changed less, and the height of the bulge had a certain influence on the force of the universal joint.

### 3.5. The Effect of the Turning Radius on the Robot

Submarine oil and gas pipelines are often laid on the seabed far away from marine life. However, due to the complex topography of a seabed, pipelines are also laid at different

turning angles, and different turning radii have a greater impact on the jamming and movement rules of the robot. Taking the two-section pipeline robot with an inner diameter of 50 mm as an example, the same pressure was passed at the inlet. Simulations were carried out for pipes with turning radii of 300, 400, 500 and 600 mm. ADAMS was used to establish the model, the leather bowl and the main body of the robot were connected by a fixed connection and the nodes were connected by a universal pair. In order to study the changing law of the robot's motion velocity and joint force under different pipe diameters, an elastic contact was set between the leather bowl and the tube wall; the friction coefficient was 0.8, and the recovery coefficient was 0.3. A 300 mm turning radius was simulated, and its motion speed is shown in Figure 17. The force at the center of the cross is shown in Figure 18.



**Figure 17.** The robot's movement speed at a 300 mm turning radius.

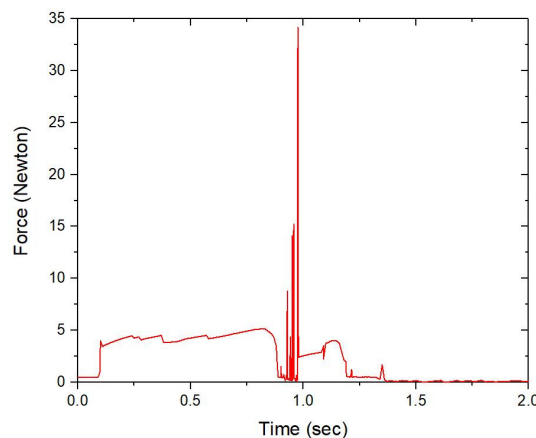


**Figure 18.** Force at the connection point of the robot with a turning radius of 300 mm.

When the turning radius of the pipeline was 300 mm, its speed changed, as shown in Figure 17. The initial pressure of the inlet robot was set to 5 MPa and remained unchanged. At the moment of turning, the pipeline robot was blocked under the action of the contact force. With an increase, the pipeline robot obtained instantaneous speed. Due to the direct effect of the pressure on the back end of the robot, its instantaneous speed was slightly greater than the speed of the front end of the robot, and the speed could reach 1.5 m/s. When entering the transition section of the curve, the jam phenomenon occurred again. In addition, due to the effect of the rear pressure, the pipeline robot started again, and the average speed reached 2.5 m/s. After cornering, the pipeline robot had a constant speed fluctuation to achieve an obvious vibration effect. Due to the direct force on the rear section, the vibration of the rear of robot was more obvious. Figure 18 shows the force on the coupling part connecting the front and rear cabins during the operation of the pipeline robot. The force in the two periods before and after the bend was small and could be ignored. Only the maximum force at the connection point occurred at the moment of the

bend damage to the robot. To sum up, when the turning radius of the pipeline was 300 mm, it was regarded as the minimum critical value of the robot's passability. Jamming during its operation can occur easily, and the maximum force on the coupling can easily cause the multisection pipeline robot to break. Therefore, a pipe with a 300 mm turning radius was not feasible. Thus, a simulation analysis was carried out on pipes with a turning radii of 400, 500 and 600 mm. After the comparison, the forces at the connection points of the three were roughly the same. Taking a 400 mm turning radius as an example, the force components along the  $y$ -axis (vertical direction) and  $z$ -axis (horizontal direction) at the connection point are shown in Figure 19.

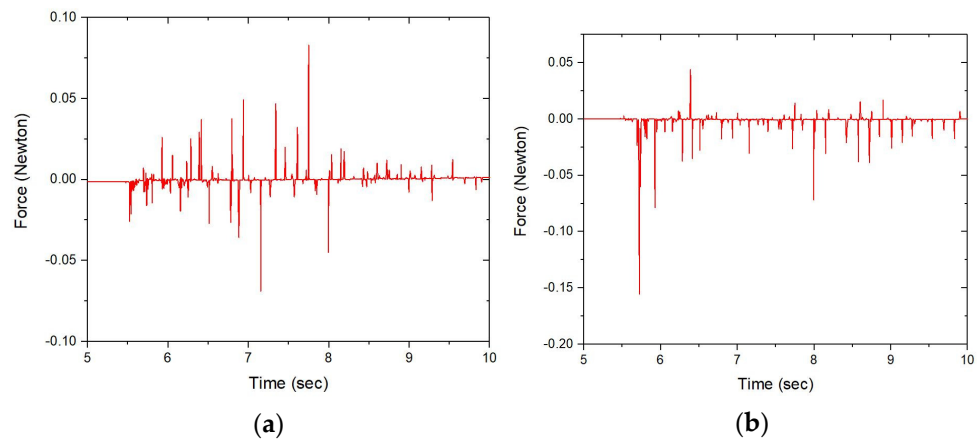


**Figure 19.** The force along the  $y$ -axis and the  $z$ -axis at the connection point of the robot, with a 400 mm turning radius: (a) 400 mm  $z$ -axis force; (b) 400 mm  $y$ -axis force.

After comparing the results of the three sets of simulations, the force changes at the pipeline robot connection point were seen to be small and approximately the same. It indicates that the change in the turning radius over the minimum critical value has little effect on the force of the coupling. According to the above figure, Figure 19a shows the force on the connection point along the  $z$ -axis when the robot was cornering, and it was also the tangential force along the pipe section. The positive direction of the  $z$ -axis is the pulling force along the outside of the pipe. Conversely, it is the thrust along the inner pair of the pipe. As shown in the figure, the two forces in the  $z$ -axis direction were relatively uniform and cancelled each other out during the turning process. During the rotation, the coupling reciprocates inward and then outward, and the force increases and then decreases. It means that the angle of motion increases first and then decreases. The swing angle of the coupling is the largest in the turning transition section. Figure 19b shows the force on the connection point along the  $y$ -axis when the robot was cornering, which was also the normal force along the pipe section. The positive direction of the  $y$ -axis was the reverse friction force of the cup during operation. In the opposite direction, the drag force is generated under the influence of the rear pressure. As shown in the figure, the friction force always existed during the operation, and the friction force changed greatly at the moment of entering and exiting the bend pipeline. However, during the motion, the drag force of the robot is much greater than the friction force of the leather bowl. This ensured that the pipeline robot successfully completed the pigging task with minimal damage to the robot.

Ensuring that the initial force of the pipeline robot remained unchanged, the speed fluctuation and vibration effect of the pipeline robot under the three groups of different turning radii were analyzed. Ensuring that the elastic contact between the leather bowl and the tube wall, the friction coefficient and the recovery coefficient were unchanged, and the same pressure was passed into the entrance. The simulation results are shown in Figures 20 and 21.

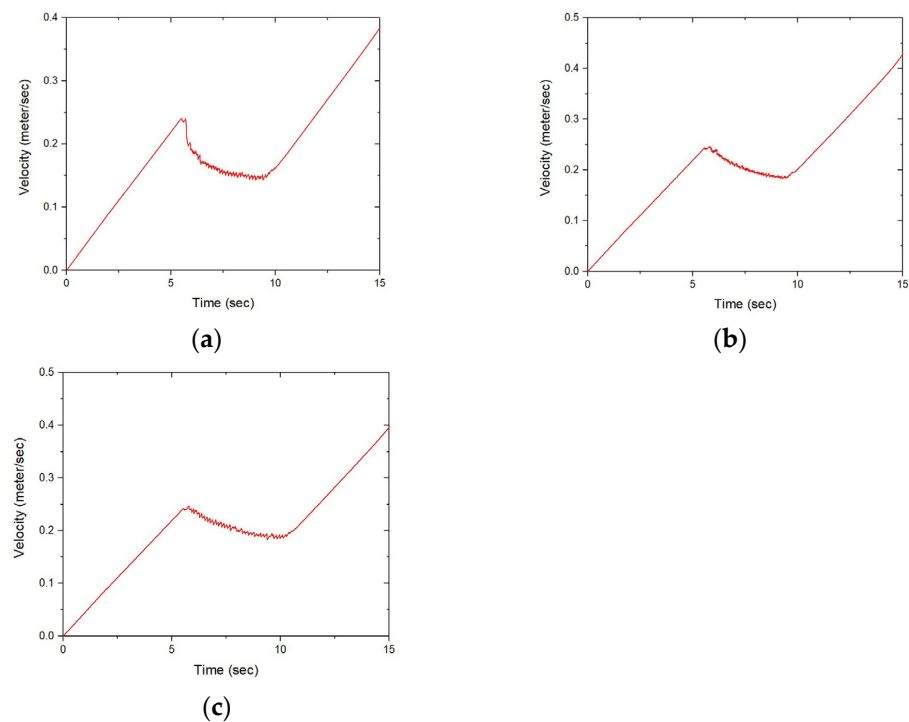


**Figure 20.** Robot movement speed with different turning radii: (a) 400 mm robot movement speed; (b) 500 mm robot movement speed; (c) 600 mm robot movement speed.

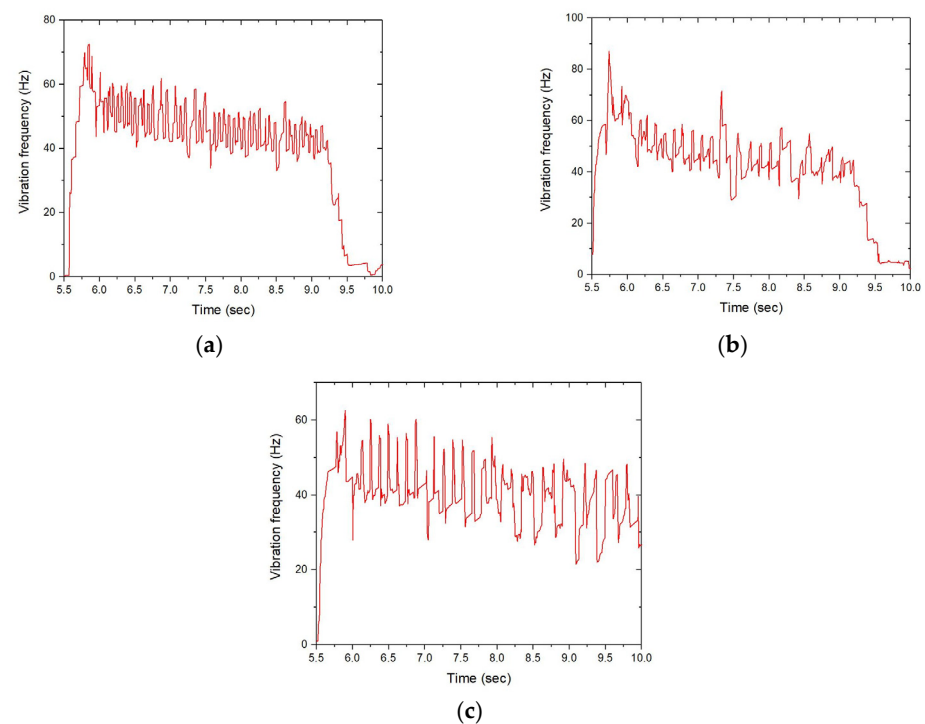


**Figure 21.** The vibration frequency of the robot with different turning radii: (a) 400 mm robot vibration frequency; (b) 500 mm robot vibration frequency; (c) 600 mm robot vibration frequency.

According to the comparison and analysis of the three sets of data, the speed of the pipeline robot before entering the bend and after exiting the bend was approximately the same for pipeline conditions with different turning radii. Only the speed through the bend was slightly different. When the turning radius was 400 mm, the robot slowed down significantly when entering the curve, the minimum speed reached 0.14 m/s and the speed

fluctuated greatly in the transition section of the curve. When the turning radius was 600 mm, the robot decelerated gently when entering the curve, the minimum speed reached 0.18 m/s and the speed fluctuation in the transition section of the curve was small. Since the speed fluctuation of the robot in the transition section generated vibration, according to the comparison of the vibration images, the average vibration value of the three groups was kept at approximately 50 Hz, but the vibration amplitude of the 400 mm turning radius changed the most, and the fluctuation rate was the fastest, while the 600 mm turning radius had the smallest change in the vibration amplitude, and the fluctuation rate was relatively slow. To sum up, the speed fluctuation and vibration frequency decreases with the increase in the pipe turning radius.

#### 4. Mechanical Properties Experiment

In order to deeply study the operation rules and the mechanical characteristics of the single-section and multisection pipeline robots, an experimental device was designed and built to simulate the operation of the pipeline robots under actual working conditions. By changing the length of the pipe robot and the number of leather cups, as well as increasing the number of compartments, the influence of the different structures on the speed of the pipe robot passing through the pipe was analyzed. At the same time, by calculating the resistance of the different types of pipeline robots during movement, the influence of the structural change on the contact force between the cup and the pipe wall was analyzed.

##### 4.1. Test Bench Construction

The design of the pipe robot bending test bench is shown in Figure 22. A multilayer pipeline test bench was built, and a tube support to fix the iron tube and the transparent glass tube on the iron frame was used. The pumping process was realized by the console so that the liquid circulated in the pipeline. A ball device was used to make the pipeline robot enter the pipeline and move under the drive of the liquid. Three sensors were distributed on each pipeline to measure the pressure difference between the front and rear of the pipeline robot, and the data were directly received by the console. The speed was detected by a high-speed camera, and the running resistance could be calculated after calculating the average acceleration. Experiments were carried out by changing the number of the pipe robot cups, the length of the pipe robot and the number of the pipe robot cabins. The relationship between the running speed, the number of compartments and the number of cups and the contact force of the pipeline robot under the liquid phase drive was explored. The entire pipeline was divided into four observation areas: A, B, C and D. Three pressure sensors were installed on the pressure curve corresponding to three observation points. To achieve lubrication, a bypass was designed at the robot end of the pipe. The fluid was allowed to flow through the bypass into the pipe before each test to reduce testing errors. The experimental bench and robot parameters are shown in Tables 2 and 3.



Figure 22. Test bench construction.

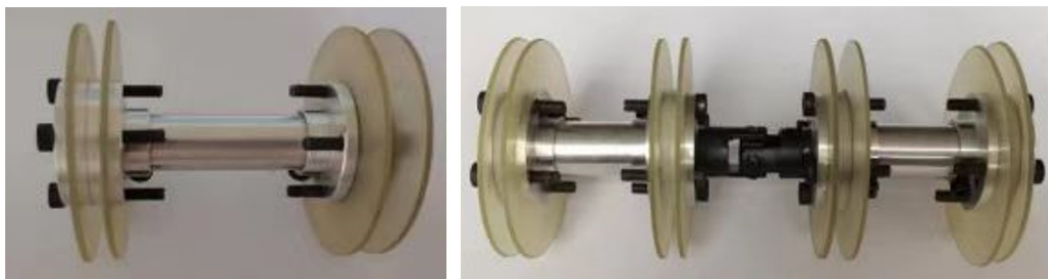
**Table 2.** Piping laboratory equipment.

Component	Material/Model	Quantity
Straight pipe	Acrylic glass/stainless steel	4
Bend pipe	Acrylic glass/stainless steel	4
Pipe-fixing clip	Stainless steel	8
Controlled pressure pump	CDMF10-8FSWSC	1
Pressure sensor	MIK-P300	13
Flowmeter	Caliber DN25	1
Flow control valve	Caliber DN50	1

**Table 3.** Pipeline robot components.

Component	Material	Size (mm)
Flange	Aluminum alloy	10
Core tube	Aluminum alloy	60
Leather bowl	Polyurethane	25
End cap	Aluminum alloy	10

Figure 23 shows the equipment required for the test bench and the physical map of the single-cabin pipeline robot and the double-cabin pipeline robot. The robot consisted of a flange, an end cover, a cup and a core tube, and it was connected with M3 screws. The coupling and the front and rear cabin sections were fixed by welding. The overall mass of the single-section pipeline robot was 39.4 g, and the mass of the two-section pipeline robot was 80 g. The motion speed of the robot was recorded by a high-speed camera to record each movement process and movement time. By measuring the length of the different test segments, the motion speed between the different test segments could be measured.

**Figure 23.** Pipe robot model.

#### 4.2. Influence of the Robot's Length on the Cornering

In order to explore the influence of the length of the pipeline robot on turning, pipeline robots with different cabin lengths were selected. The lengths of 1.2D, 1.3D and 1.4D were taken, respectively, as 60, 65 and 70 mm, and the drive in the pipeline under the same flow and pressure was as shown in Figure 24. According to the statistics obtained from the pressure sensor, the pressure in the empty pipe after passing water was 0.007 MPa. When the pipe robot with a length of 60 mm was put into the pipe, the pressure sensor showed that the pressure in the pipe increased to approximately 0.016 MPa. A pressure image for each observation area is shown in Figure 25.

The pressure profile of the robot through the four positions as shown in Figure 25. The shorter robots had more significant pressure changes after a period of motion. As shown in Figure 26, the 1.2D pipeline robot had the fastest acceleration in the straight pipe; the speed when passing by the third sensor was 4.45 m/s, and the speed reduced to 1.3 m/s after passing by the fifth sensor after 0.5 s. The acceleration was  $-6.33 \text{ m/s}^2$ , and the resistance reached the maximum. The speed of the 1.3D pipeline robot increased to 3.96 m/s through the third sensor in the straight pipe and passed through the fifth

sensor after 0.7 s; the speed decreased to 0.97 m/s, and the acceleration was  $-4.25 \text{ m/s}^2$ . The maximum acceleration of the 1.4D pipeline robot was  $-0.79 \text{ m/s}^2$ ; the speed reached 1.48 m/s after passing through the third sensor, and the speed decreased to 0.79 m/s after passing through the fifth sensor in 0.6 s. The 1.2D pipeline robot had the fastest speed in the whole process, with the smallest bending acceleration, and the contact force between the cup and the pipe wall was the largest during bending. The 1.4D pipeline robot was the slowest in the whole process and had the largest bending acceleration. The indirect contact force was minimal. Experiments have shown that the motion speed gradually decreases as the robot becomes more massive with greater length. During the cornering phase, the shorter robot has a greater variation in speed and is subjected to a greater contact force due to frictional forces. Therefore, the longer the length, the smoother the motion and the lower the contact force, provided that the robot meets the conditions for passing through the pipe.

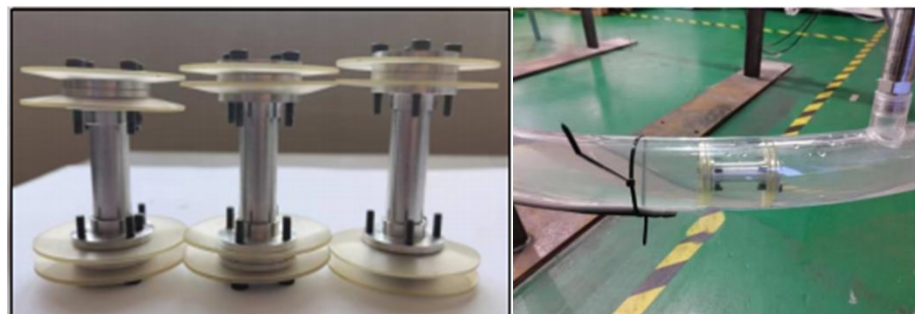


Figure 24. Pipeline robot with two-cup, four-cup and six-cup.

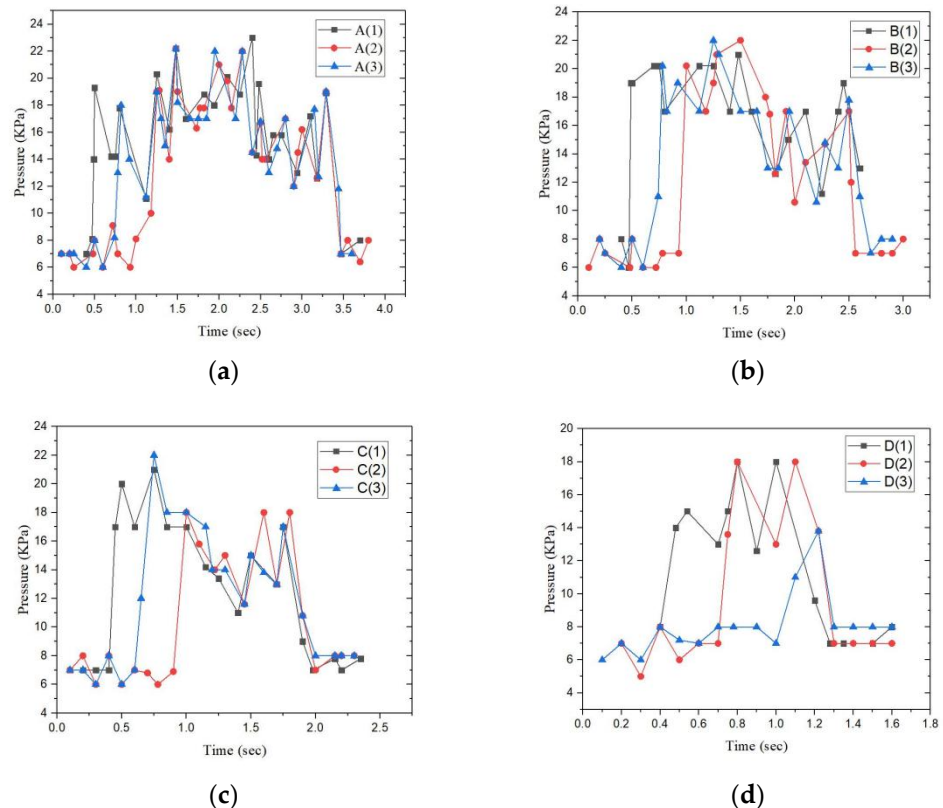
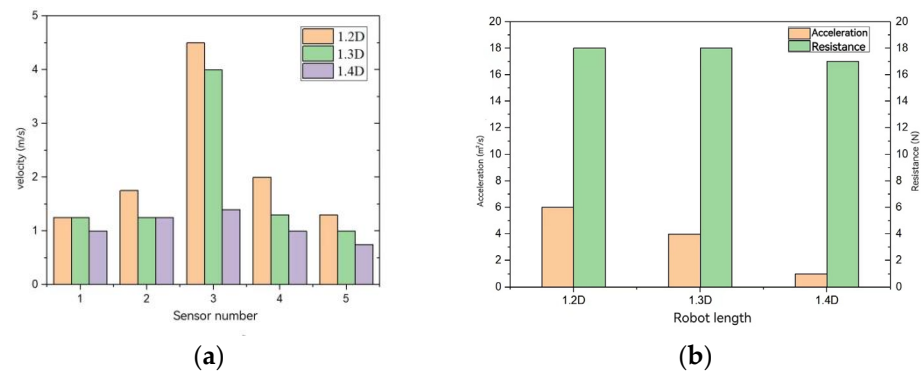


Figure 25. Pressure images of the different robot lengths at the A, B, C and D observation points: (a) Point A pressure curve; (b) Point B pressure curve; (c) Point C pressure curve; (d) Point D pressure curve.



**Figure 26.** Variations in the velocity of the different robot lengths at the A, B, C and D observation points: (a) Different types of robots vary in speed at different positions; (b) Acceleration and resistance for different types of robots.

#### 4.3. The Influence of the Number of Cups on the Robot

In order to verify the influence of the number of cups of the pipeline robot on cornering in the simulation, the number of cups was changed, as shown in Figure 27.

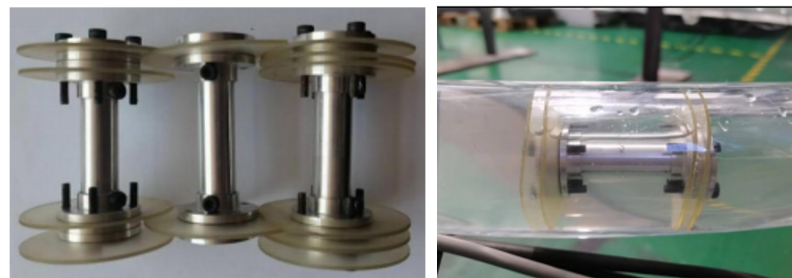


**Figure 27.** Robot models with different numbers of cups.

The two-cup, four-cup and six-cup pipeline robots were run in the pipeline at the same flow and pressure. The speed of the pipeline robot was calculated by observing the time when the pressure value changed at the point. After the water passed through the empty pipe, the pressure was 0.007 MPa. The pipe robot with six cups was put into the pipe to run, and the pressure sensor showed that the pressure in the pipe increased to approximately 0.020 MPa. Figure 28 shows the pressure image of the six-cup pipeline robot passing through each observation area.

The pressure curve of the robot passing through the monitoring point with different number of leather bowls as shown in Figure 28. The robot with six-cup had a large pressure change after a period of movement. The higher the number of leather bowls, the higher the friction, and the higher the pressure generated. As shown in Figure 29, the speed of the pipeline robot with double cups was 5 m/s when it passed the third sensor, and the speed reduced to 1.9 m/s when it passed the fifth sensor after 0.3 s. The minimum acceleration was  $-10.13 \text{ m/s}^2$ , and the resistance reached the maximum. The pipeline robot with four cups passed through the third sensor at a speed of 3.95 m/s and passed through the fifth sensor after 0.7 s. The speed reduced to 0.97 m/s, and the acceleration was  $-4.26 \text{ m/s}^2$ . After passing through the third sensor, the pipeline robot with six cups reached a speed of 2.22 m/s and passed through the fifth sensor in 0.8 s. The speed reduced to 0.98 m/s, and the acceleration was  $-1.56 \text{ m/s}^2$ . The two-cup pipeline robot was the fastest in the whole process, with the smallest bending acceleration, and the contact force between the leather cup and the pipe wall was the largest during bending. The six-cup pipeline robot ran the slowest in the whole process and had the largest bending acceleration. Experiments have shown that, with the increase in the number of leather bowls, the friction force with the tube wall during the movement increases and the movement speed is slower. However, in the case of small leather bowl overflow, the more stable the robot movement with more

leather bowls, and the better the pipe-clearing effect, the smaller the contact force with the pipe wall and the smaller the wear of the leather bowls.

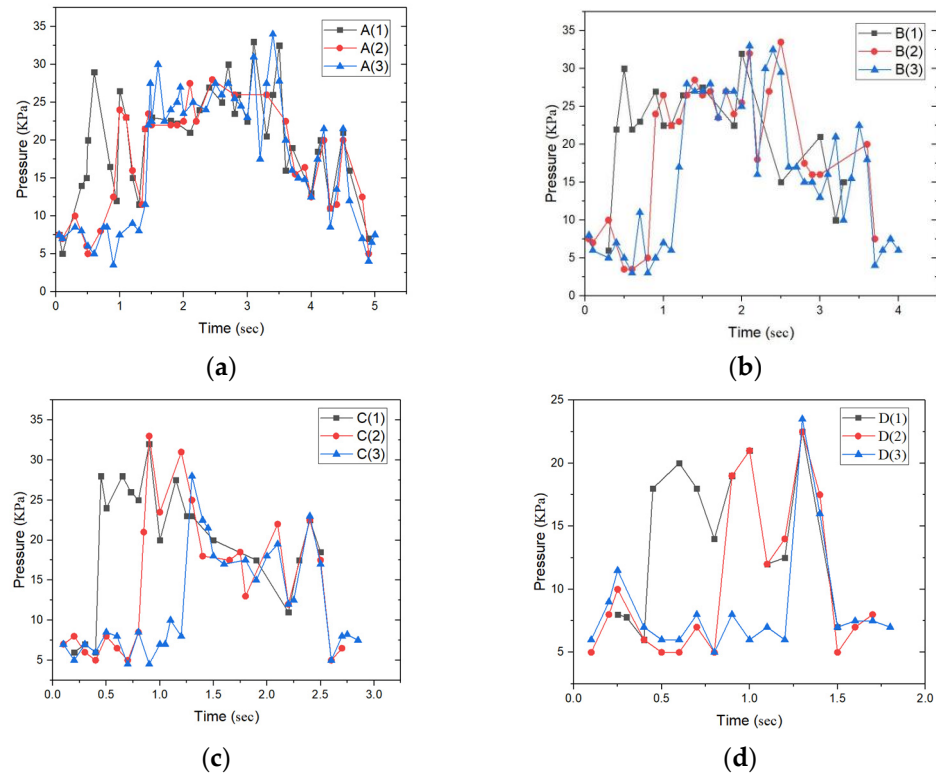


**Figure 28.** Pressure of the different numbers of cups at the A, B, C and D monitoring points: (a) Point A pressure curve; (b) Point B pressure curve; (c) Point C pressure curve; (d) Point D pressure curve.

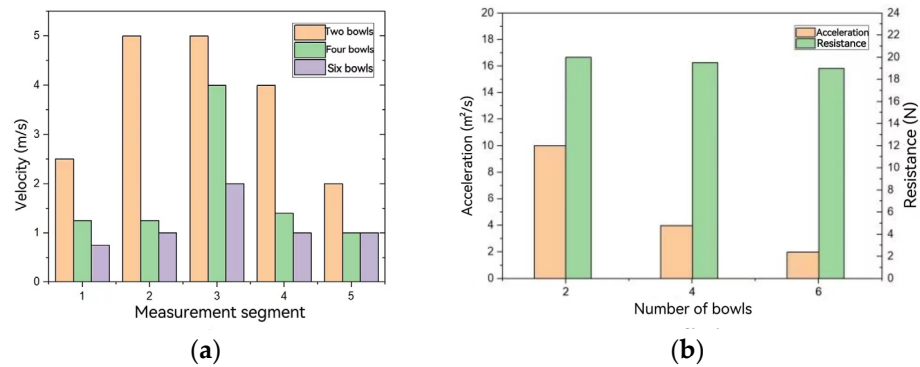


**Figure 29.** Movement speed of the different numbers of cups at the A, B, C and D monitoring points.: (a) Different types of robots vary in speed at different positions; (b) Acceleration and resistance for different types of robots.

#### 4.4. Cornering Characteristics of the Two-Section Robot

In order to verify the difference between the two-section robot and the single-section robot in the simulation, the pipeline was added. The robot cabin segments were connected by universal couplings, and the two-section pipeline robot is shown in Figure 30.

The two-section pipeline robot moves through the pipeline at the same flow rate and pressure. Figure 31 shows the pressure images of the two-section robot passing through each observation area. After the water passed through the pipeline, the pressure was 0.007 MPa. When the pipeline robot was running in the pipeline, the pressure sensor showed that the pressure in the pipeline increased to approximately 0.035 MPa.



Figure 30. Double-cabin robot model.

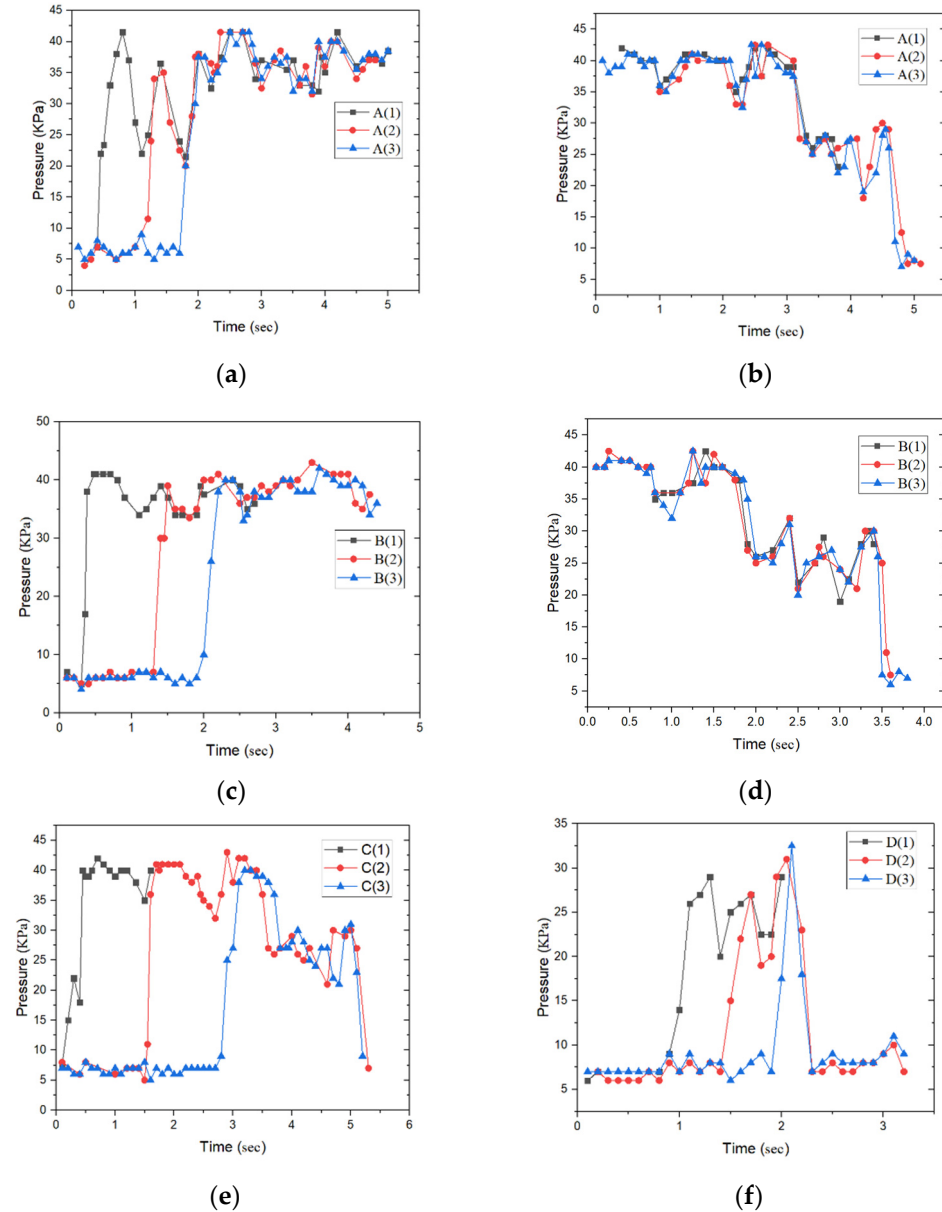
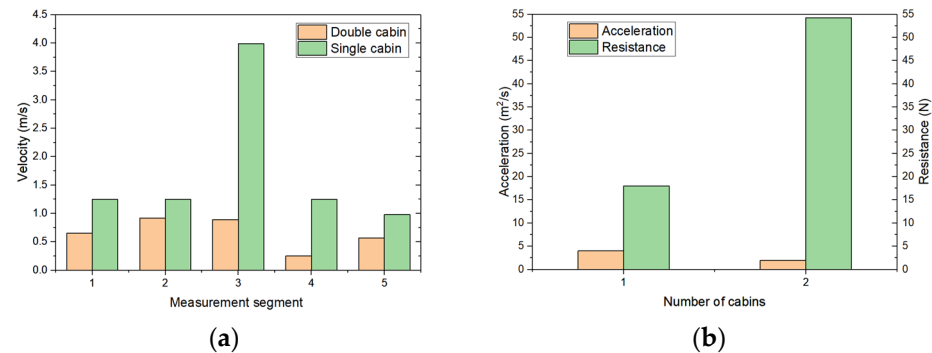


Figure 31. Pressure changes of the two-cabin robot at the different monitoring points (A, B, C and D): (a) Front section robot A point pressure curve; (b) Back section robot A point pressure curve; (c) Front section robot B point pressure curve; (d) Back section robot B point pressure curve; (d) Front section robot B point pressure curve; (e) Point C pressure curve; (f) Point D pressure curve.

The pressure curve of the two-section pipeline robot passing through the monitoring point as shown in Figure 31. In the AB interval, the pressure in the two compartments of the robot is opposite, and the pressure is maximum at the connection point. During a period of motion past point D, the pressure leveled off.

The high-speed camera was used to capture images of the robot entering and leaving the test section. The time was calculated based on the frequency of each frame taken. The running time of the double-section pipeline robot was 9.4 s, while the single-section robot was 3 s. The running speed of the single-section robot was much higher than that of the two-section robot. The straight pipes and elbows in the AB area were selected for specific analysis. The time for the pipeline robot to pass the pressure sensor, the speed of each node, the average acceleration of the elbow section and the resistance when the pipeline robot of each length passed through the bend were calculated. The results are shown in Figure 32.



**Figure 32.** Movement speed of the robots in different cabins: (a) Different types of robots vary in speed at different positions; (b) Acceleration and resistance for different types of robots.

As shown in the figure, the speed of the dual-cabin section robot was 0.893 m/s when it passed the third sensor, and the speed reduced to 0.57 m/s when it passed the fifth sensor after 1.7 s. The acceleration was  $-1.19 \text{ m/s}^2$ , and the resistance was 54.26 N. The whole movement process was slow compared to the single-section pipeline robot. Experiments have shown that, as the number of compartments increases, the robot mass increases, while the front and rear compartments generate reaction forces under the action of the coupling. Therefore, its motion is slow, and the resistance is greater.

## 5. Conclusions

Through the simulation analysis in this paper, the motion laws of the robots with multiple cabins were shown to be roughly the same, but the movement speed of the three-cabin section robot was very slow. It can be seen that, with the increase in the number of cabins, the overall gravity increases; the increase in the number of cups leads to friction. The force increases, making the movement slower. At the same time, the more cabins there are, the greater the torque the universal joint bears when it enters the curve, which is likely to cause the curve to become blocked. Before the robot goes through the bend, due to the influence of gravity, the normal force along the pipe wall is large and accompanied by obvious vibration. The force is obvious, and the speed fluctuates rapidly, resulting in weak vibration.

By changing the height of the bulge, it was found that the different heights have a great influence on the motion law of the robot when cornering. The force change at the universal joint was the largest. When the front cabin section passed through the bulge, the universal joint had the maximum torque, and the stress reached 43 MPa. Second, the contact stress at the cup had a large change, and the first cup bore the maximum stress up to 5.5 MPa. By analyzing different turning radii, it was found that the setting of the turning radius had to be at least  $6D$  to pass the pipeline smoothly. When the inner diameter of the pipeline was 50 mm, and the turning radius was at the minimum critical value of 300 mm, the vibration was obvious, jamming occurred and the machine was easily damaged. When it reached more than  $6D$ , with the increase in the turning radius, the speed tended to be stable and the vibration was small, indicating that the working efficiency of the robot was higher.

Through this research, firstly, experiments were carried out with different lengths of cabin sections. The experiments showed that the longer the cabin section length, the

greater the required pressure drive, the slower the movement speed and the greater the time consumption. Secondly, three groups of leather cups with different numbers were used for the experiment. With the increase in the number of leather cups, the interval between the leather cups gradually narrowed. The results show that, under the same pressure and flow conditions, the greater the number of cups, the smaller the interval rate, the greater the friction, the slower the movement speed, and the best working effect is when the interval rate is kept at 7%. Finally, an experiment on the cornering characteristics of the double-cabin section robot was carried out. Compared with the single-section robot, the speed of the two-section robot obviously met resistance at the cornering stage, which could reach 54.2 N, and the speed was very slow.

**Author Contributions:** Conceptualization, S.C.; methodology, S.C.; software, K.T. and M.Z.; validation, K.Z.; formal analysis, K.T. and K.Z.; investigation, K.T. and X.W.; resources, S.C.; data curation, L.X.; writing—original draft preparation, K.T.; writing—review and editing, M.Z. and Y.Z.; visualization, S.C. and X.W.; supervision, K.Z. and Y.G.; project administration, L.X.; funding acquisition, S.C. All authors have read and agreed to the published version of the manuscript.

**Funding:** This work was supported by the National Natural Science Foundation of China (U1908228).

**Data Availability Statement:** We excluded this statement, and the study did not report any data.

**Acknowledgments:** The author contribution or funding sections have covered all support.

**Conflicts of Interest:** The authors declare that they have no known competing financial interest or personal relationship that could have appeared to influence the work reported in this paper.

## References

- Peng, H. Design and Simulation Experiment of Gas Pipeline Crawling Robot. *J. Shenyang Univ. Technol.* **2021**, *43*, 48–49.
- Kaneko, M.; Hiyamizu, K.; Tsuji, T.; Imamura, N. Dynamic behavior of pipe inspection robot driven by fluid force. *Trans. Jpn. Soc. Mech. Eng.* **1997**, *63 Pt C*, 2368–2376. [[CrossRef](#)]
- Sakakibara, N.; Kyriakides, S.; Corona, E. Collapse of partially corroded or worn pipe under external pressure. *Int. J. Mech. Sci.* **2008**, *50*, 1586–1597. [[CrossRef](#)]
- Liu, Y.H.; Cen, Z.Z.; Chen, H.F.; Xu, B.Y. Plastic collapse analysis of defective pipelines under multi-loading systems. *Int. J. Mech. Sci.* **2000**, *42*, 1607–1622. [[CrossRef](#)]
- Ye, H.; Qian, J.; Yan, S.; Jiang, C.; Wei, L.; Jin, Z.-J. Limit bending moment for pipes with two circumferential flaws under combined internal pressure and bending. *Int. J. Mech. Sci.* **2016**, *106*, 319–330. [[CrossRef](#)]
- Yang, Y.M.; Huang, W.M. Mechanical structure design of energy self-sufficient pipeline robot. *J. Robot* **2006**, *28*, 327–330.
- Vik, M.A.; Kristiansen, A.A.; Sykes, S.S. Multi-Diameter, Bi-Directional Pigging for Pipeline Pre-Commissioning. In Proceedings of the C. Pigging Products and Services Association Seminar, Aberdeen, UK, 17 February 2010.
- Idelchik, L.E.; Kolesnikov, A.V. *Handbook of Hydraulic Resistance*; Hemisphere Publishing Corp.: Washington, DC, USA, 1986. [[CrossRef](#)]
- Zhu, X.; Zhang, S.; Tan, G.; Wang, D.; Wang, W. Experimental study on dynamics of rotatable bypass-valve in speed control pig in gas pipeline. *Measurement* **2014**, *47*, 686–692. [[CrossRef](#)]
- Chen, J.; Luo, X.; Zhang, H. Experimental study on movement characteristics of bypass pig. *J. Nat. Gas Sci. Eng.* **2018**, *59*, 212–223. [[CrossRef](#)]
- Granosik, G.; Borenstein, J. Integrated joint actuator for serpentine robots. *J. IEEE/ASME Trans. Mechatron.* **2005**, *10*, 473–481. [[CrossRef](#)]
- Kwon, Y.-S.; Lee, B.; Whang, I.-C.; Yi, B.-J. A pipeline inspection robot with a linkage type mechanical clutch. In Proceedings of the 2010 IEEE/RSJ International Conference on Intelligent Robots and Systems, Taipei, Taiwan, 18–22 October 2010; IEEE: Piscataway, NJ, USA, 2010; pp. 2850–2855.
- Kakogawa, A.; Ma, S. Stiffness Design of Springs for a Screw Drive In-Pipe Robot to Pass through Curved Pipes and Vertical Straight Pipes. *J. Adv. Robot.* **2012**, *26*, 253–276. [[CrossRef](#)]
- Gleicher, S.C.; Chamecki, M.; Isard, S.A. Interpreting three-dimensional spore concentration measurements and escape fraction in a crop canopy using a coupled Eulerian–Lagrangian stochastic model. *J. Agric. For. Meteorol.* **2014**, *194*, 118–131. [[CrossRef](#)]
- Ducobu, F.; Rivière-Lorphèvre, E. Application of the Coupled Eulerian-Lagrangian (CEL) method to the modeling of orthogonal cutting. *J. Eur. J. Mech.* **2016**, *59*, 58–66. [[CrossRef](#)]
- Xue, X.Y. Research on Running Characteristics of Pipeline Robot Driven by Fluid Pressure. Master’s Thesis, Institute of Mechanical Engineering, Harbin Engineering University, Harbin, China, 2017.
- Hendrix, M.; Graafland, C. Frictional forces for disc-type pigging of pipelines. *J. Pet. Sci. Eng.* **2018**, *171*, 905–918. [[CrossRef](#)]

18. Goharimanesh, M.; Mehrkish, A.; Janabi-Sharifi, F. A fuzzy reinforcement learning approach for continuum robot control. *J. Intell. Rob. Syst.* **2020**, *100*, 809–826. [[CrossRef](#)]
19. Ignacio, C.; Mariano, D.P.; Gerardo, G.A. An adaptive deep reinforcement learning approach for MIMO PID control of mobile robots. *ISA Trans.* **2020**, *102*, 280–294. [[CrossRef](#)]
20. IJsseldijk, H.P. By-Pass Pigging—Experiments and Simulations. Master’s Thesis, Delft University of Technology, Delft, The Netherlands, 2016.
21. Mirshamsi, M.; Rafeeyan, M. Dynamic analysis and simulation of long PIG in gas pipeline. *J. Nat. Gas Sci. Eng.* **2015**, *23*, 294–303. [[CrossRef](#)]
22. Lima, G.F.; Freitas, V.C.G. Pig’s speed estimated with pressure transducers and hall effect sensor: An industrial application of sensors to validate a testing laboratory. *Sensors* **2017**, *17*, 2119. [[CrossRef](#)]
23. Naeini, H.S. Experimental investigation on sphere PIG movement in multiple thickness pipe. *J. Nat. Gas Sci. Eng.* **2021**, *95*, 104152. [[CrossRef](#)]
24. Cheng, L.L.; Yang, Y.M. Dynamics stability of the micro robot moving in bent pipe. *Control Theory Appl.* **2001**, *18*, 62–68.
25. Xu, F.P.; Deng, Z.Q. Research on traveling-capability of pipeline robot in elbow. *Robot* **2004**, *26*, 155–160.
26. Wang, W.M.; Song, S.N.; Zhang, S.M.; Yu, D. Impact analysis of pigging in shield segment of gas pipe. In Proceedings of the IEEE International Conference on Mechatronics and Automation, Chengdu, China, 5–8 August 2012; IEEE: Piscataway, NJ, USA, 2012; pp. 203–207.
27. Zhang, H.; Li, Q.; Liu, S.H. Influence of the thickness of the rubber cup of a large pig pig on its stiffness characteristics. *J. Oil Mine Mach.* **2015**, *44*, 12–18.
28. Zhang, H.; Liu, S.H.; Li, Q. Influence of 1016 mm pig sealing cup interference on its stiffness characteristics. *J. Chem. Equip. Pipelines* **2015**, *52*, 82–86.
29. Zhang, H.; Wang, Y.; Zhang, S.M.; Zhang, K. Finite Element Analysis of Mechanical Properties of Pig Sealing Cups. *J. Gas Storage Transp.* **2015**, *34*, 1225–1230.
30. Zhang, H.; Zhang, S.M.; Guo, S.D. Dynamic Simulation of the Process of Straight Plate Pig Passing through the Circumferential Weld. *J. Oil Mine Mach.* **2015**, *44*, 22–27.
31. Zhang, S.M.; Zhu, X.X. Finite-element analysis on mechanical properties of sealing disc for pig. *J. Oil Gas Storage Transp.* **2015**, *34*, 1225–1230.
32. Hosseina Lipour, S.M.; Zarif Khalili, A.; Salimi, A. Numerical simulation of Pig Motion through Gas Pipelines. *J. Iran Univ. Sci. Technol.* **2007**, *12*, 2–7.
33. Zhu, X.; Wang, D.; Yeung, H. Comparison of linear and nonlinear simulations of bidirectional pig contact forces in gas pipelines. *J. Appl. Fluid Mech.* **2015**, *27*, 151–157. [[CrossRef](#)]
34. Zhu, X.; Zhang, S.; Li, X. Numerical simulation of contact force on bi-directional pig in gas pipeline: At the early stage of pigging. *J. Nat. Gas Sci. Eng.* **2015**, *23*, 127–138. [[CrossRef](#)]
35. Den Heijer, A. Frictional Behaviour of Pigs in Motion. Master’s Thesis, Delft University of Technology, Delft, The Netherlands, 2016.
36. Liang, Z.; He, H.G.; Cai, W.L. Speed simulation of bypass hole PIG with a brake unit in liquid pipe. *J. Nat. Gas Sci. Eng.* **2017**, *42*, 40–47. [[CrossRef](#)]
37. Miao, X.Y.; Zhao, H. Regulating control of in-pipe intelligent isolation plugging tool based on adaptive dynamic programming. *J. Pipeline Syst. Eng. Pract.* **2022**, *13*, 04022003. [[CrossRef](#)]
38. Kim, S.; Yoo, K.; Koo, B. Speed excursion simulation of PIG using improved friction models. *J. Nat. Gas Sci. Eng.* **2022**, *97*, 104371. [[CrossRef](#)]
39. Li, X.W.; He, L.M. Numerical simulation and experimental study of bypass pigging slippage. *Ocean Eng.* **2021**, *230*, 109203. [[CrossRef](#)]
40. Liu, Y.T.; Zhu, X.X. Research on bypass pigging in offshore riser system to mitigate severe slugging. *Ocean Eng.* **2022**, *246*, 110606. [[CrossRef](#)]
41. Chen, S.T.; Zhang, Y.B. Numerical simulation and experiment of the gas-liquid two-phase flow in the pigging process based on bypass state. *Ocean Eng.* **2022**, *252*, 111184. [[CrossRef](#)]
42. Cao, Y.G.; Liu, C.; Tian, H.J.; Sun, Y.T.; Zhang, S.H. Mechanical behaviors of pipeline inspection gauge (pig) in launching process based on Coupled Eulerian-Lagrangian (CEL) method. *Int. J. Press. Ves. Pip.* **2022**, *197*, 104622. [[CrossRef](#)]

**Disclaimer/Publisher’s Note:** The statements, opinions and data contained in all publications are solely those of the individual author(s) and contributor(s) and not of MDPI and/or the editor(s). MDPI and/or the editor(s) disclaim responsibility for any injury to people or property resulting from any ideas, methods, instructions or products referred to in the content.